RSC Advances

Cite this: *RSC Advances*, 2012, **2**, 4932–4943

www.rsc.org/advances

PAPER

Improvement of transport properties and hydrogen permeation of chemically-stable proton-conducting oxides based on the system $BaZr_{1-x-y}Y_xM_yO_{3-\delta}$†

Sonia Escolástico,[a] Mariya Ivanova,[b] Cecilia Solís,[a] Stefan Roitsch,[c] Wilhelm A. Meulenberg[b] and José M. Serra*[a]

Received 7th February 2012, Accepted 18th March 2012
DOI: 10.1039/c2ra20214j

The structural and transport properties as well as the chemical stability of a series of proton-conducting oxides based on yttrium-doped barium zirconate were investigated. Specifically, Pr-, Fe- and Mn-doped $BaZr_{1-x-y}Y_xM_yO_{3-\delta}$ compounds were prepared by solid state reaction. The compound exhibiting the highest total and protonic conductivity at elevated temperatures under reducing atmospheres was $BaZr_{0.8}Y_{0.15}Mn_{0.05}O_{3-\delta}$. Temperature-programmed reduction experiments revealed a particular redox behavior related to the Mn-species under selected conditions. The hydrogen permeation was thoroughly studied as a function of the temperature, hydrogen concentration and the humidification degree in the sweep gas. Moreover, the transient processes induced by alternate step changes in the humidification degree of the sweep gas were analysed. The highest steady hydrogen evolution flow exceeded 0.03 ml min^{-1} cm^{-2} (0.9 mm-thick membrane) at 1000 °C for the humidified sweep gas. The stability of $BaZr_{0.8}Y_{0.15}M_{0.05}O_{3-\delta}$ under operation-relevant atmospheres (CO_2-rich reducing atmosphere at high temperature) was tested using different techniques (X-ray diffraction (XRD), Raman, SEM, TEM and TG) and the results showed that this material is stable even when exposed to 115 ppm H_2S.

1. Introduction

Hydrogen permeation membranes based on ceramic proton-conducting oxides[1] may enable hydrogen purification and separation at high temperature, therefore making possible a high degree of integration in different industrial processes. Their implementation in water gas shift reactors in power plants applying fuel gasification schemes, *e.g.* IGCC, is of special importance. Process intensification due to thermodynamic displacement through *in situ* hydrogen extraction allows simplification of the process scheme and leads to an increase in the overall process efficiency and sustainability. Additionally, hydrogen separation enables CO_2 sequestration in power plants operating on carbon-based fuels (fossil fuels or biomass-derived fuels). A prerequisite for membrane materials in this application is their stability at high temperatures in reducing and CO_2-rich environments, along with sufficient hydrogen permeability.

Many perovskite oxides, such as the doped $BaCeO_3$, $SrCeO_3$, $SrZrO_3$ and $BaZrO_3$ are reported to have reasonable proton conductivity in hydrogen-rich and humid atmospheres. From these groups, $BaCeO_3$-based compounds exhibit the highest conductivity,[2] however they suffer from insufficient chemical stability, especially in CO_2-containing atmospheres. Exposure to CO_2 leads to material degradation due to the formation of barium carbonate ($BaCO_3$) and cerium oxide (CeO_2).[3] Nevertheless, $BaZrO_3$-based compounds exhibit reasonable chemical stability but present lower conductivity, compared to the doped $BaCeO_3$ compounds, due to higher grain boundary transport limitations.[4,5] Moreover, the preparation of membranes made of doped $BaZrO_3$ requires high sintering temperatures to achieve appropriate densities or gas tightness, although different approaches have been proposed to circumvent this problem.[5–7] In order to achieve a compromise between proton conductivity and chemical stability, mixed solid solutions of $BaCeO_3$ and $BaZrO_3$ were developed, as reported elsewhere.[8,9]

In order to be implemented as hydrogen separation membranes, these materials ought to present mixed proton–electron conductivity with a stable proton conductivity term and a sufficient electronic conductivity term. The first strategy is to develop composite membranes comprising a mixture of the proton-conducting ceramic and another purely electronic conducting material to enhance the electronic conduction.[10] The most promising approach involves a material tailored to boost the mixed conductivity, as reported in ref. 9, where electronic transport may be enhanced by means of intrinsic doping of the materials with multivalent cations. Concretely, $BaCeO_3$ was

[a]*Instituto de Tecnología Química (Universidad Politécnica de Valencia–Consejo Superior de Investigaciones Científicas), Av. Naranjos s/n, E-46022 Valencia, Spain. E-mail: jmserra@itq.upv.es; Fax: +34963877809*
[b]*Forschungszentrum Jülich GmbH, Institute of Energy and Climate Research-IEK-1, Leo-Brandt-Str. 1, D-52425 Jülich, Germany*
[c]*Ernst Ruska-Centre for Microscopy and Spectroscopy with Electrons, RWTH Aachen University, Ahornstr. 55, 52074 Aachen, Germany*
† Electronic Supplementary Information (ESI) available. See DOI: 10.1039/c2ra20214j/

doped with Eu and Sm by Wachsman *et al.*, and as a result the ambipolar conductivity and hydrogen permeation were improved.[11–13] Other important works have explored the doping of $(Ba,Sr)CeO_3$ with Tb,[14] Tm,[15] Yb[16] and Nd.[17] A recent study[18] on thin supported membranes manufactured from Eu-doped $Sr(Zr,Ce)O_3$ solid solutions, reports peak hydrogen flow exceeding 0.5 ml min^{-1} cm^{-2} at 900 °C for a 20 μm-thick membrane. Recently, systematic studies[19–21] on barium zirconate have illustrated the high potential of these materials for practical application as hydrogen membranes and ceramic proton-conducting fuel cell components.

In this work, the effect of B-site partial substitution in the perovskite-structured $BaZr_{0.9}Y_{0.1}O_{3-\delta}$ material on ionic and electronic conductivity was studied. As a reference compound, the state-of-the-art protonic conductor $BaZr_{0.9}Y_{0.1}O_{3-\delta}$ was selected due to its high *bulk* protonic conductivity,[22,23] although the conductivity in polycrystalline samples drops due to the high grain boundary resistance reported for this material.[24–27] Since hydrogen permeation requires mixed proton–electron conductivity, the structure and electrical properties of the reference material were modified by incorporating different cations (Fe, Mn and Pr) with variable oxidation states on the B-site position in the perovskite, aiming to improve the electronic conductivity. Moreover, the incorporation of these elements could also affect the grain boundary resistance by decreasing it. The present contribution shows a structural study of these compounds, their electrical conductivity under operating conditions, their stability under application-oriented atmospheres and the H_2-permeation of a selected compound.

2. Experimental

2.1. Sample preparation

The solid state reaction method was used for the manufacturing of the compounds in the series $BaZr_{1-x-y}Y_xM_yO_{3-\delta}$ studied in this work. For this purpose, $BaCO_3$, ZrO_2, Y_2O_3 and the corresponding metal oxides were weighed in stoichiometric proportions, thoroughly mixed and ball milled for 10 h. Subsequent calcination followed at 1400 °C for 32 h, and the resulting materials were ball milled for 1 day using zirconia balls.

Rectangular bar samples used in the electrochemical study were prepared from the resulting $BaZr_{1-x-y}Y_xM_yO_{3-\delta}$ (where $x = 0.1$ when $y = 0$, 0.05 and $x = 0.15$ when $y = 0.05$) powders *via* uniaxial pressing at 100 MPa. The green geometry of the bars was 40 × 5 × 4 mm^3. The samples were sintered in air at 1700 °C for 30 h, obtaining a density of about 99%, as determined by the Archimedes method.

For the permeation tests in the present work, disc shaped samples with a diameter of 15 mm (in the sintered state) were uniaxially pressed at 72 MPa and sintered at 1700 °C for 30 h in air. Both disc sides were coated by screen printing with a 20 μm layer of Pt ink (Mateck, Germany), aiming to improve surface catalytic behavior. Pt coatings are not connected on the side.

2.2. Characterisation techniques

Structural and microstructural characterization. In order to control the crystallographic symmetry and phase purity of the manufactured compounds, XRD analysis was carried out on the synthesized powders by means of PANalytical CubiX FAST equipment with monochromatic Cu-Kα radiation (λ = 1.5406 Å). XRD patterns were recorded in the 2θ-diffraction angle range from 20° to 70° and analyzed using *Highscore* Philips software.

The microstructure of the sintered samples was characterized by means of scanning electron microscope Zeiss Ultra55 and transmission electron microscope FEI Tecnai F20 (with an acceleration voltage of 200 kV). TEM lamellas were prepared by means of a FIB (Focused-Ion Beam, FEI Helios Nanolab 400 s), with the subsequent thinning performed in a BAL-TEC RES-120.

Electrochemical tests. Electrical conductivity measurements were carried out by standard four-point DC technique on sintered bars. Silver paste and wires were used for contact with the samples. The constant current was supplied by a programmable current source (Keithley 2601), while the voltage drop across the sample was detected by a multimeter (Keithley 3706). The voltage was measured with the current in both forward and reverse directions, in order to eliminate the thermal effects and to avoid non-ohmic responses. Conductivity measurements were performed as a function of pO_2 in the range 2×10^{-5} to 1 atm, using different concentrations of O_2 in Ar from calibrated gas cylinders (Linde).

Furthermore, the hydration and isotopic effects were studied in: (1) dry helium and helium saturated with H_2O and D_2O; (2) dry oxygen and moist oxygen with H_2O and D_2O; (3) dry hydrogen, hydrogen saturated with H_2O, dry deuterium and deuterium saturated with D_2O. In all experiments using H_2O and D_2O, the saturation was carried out at room temperature.

Permeation tests. The sample selected for carrying out the permeation measurements was a gastight 900 μm-thick disc with a 15 mm diameter. The sealing of the sample to the supporting tube was done using gold rings. Permeation measurements were performed using a double chamber quartz reactor as schematized in Fig. 1. Hydrogen separation tests were carried out using a feed

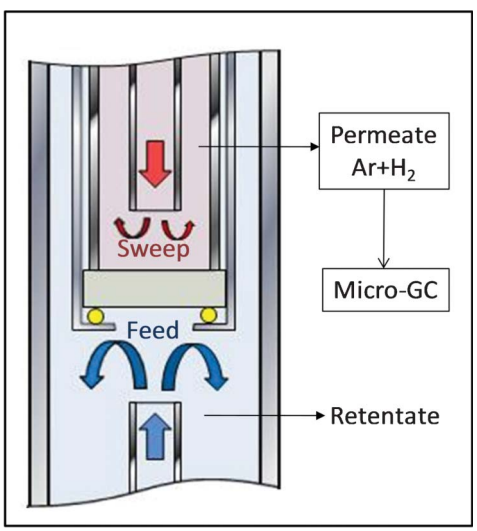

Fig. 1 Schematic illustration of the permeation rig used, having two chambers separated by a gold-sealed dense ceramic membrane.

comprising a mixture of H_2 in He (dry or saturated in water at 25 °C) and argon as the sweep gas (permeate side). The flow rates of all gas feed streams were controlled using mass flow controllers (MFCs). The flow rates were 100 ml min^{-1} cm^{-2} at the feed side and 150 ml min^{-1} cm^{-2} at the sweep side. From the hydrogen content measured on the argon side (permeate side) and the argon flow rate, the total hydrogen permeation rate was calculated, assuming the ideal gas law. The permeation fluxes in ml min^{-1} cm^{-2} were calculated by dividing the permeation rates by the effective surface area of the membrane. The hydrogen content in the permeate side was analyzed using a micro-GC Varian CP-4900 equipped with Molsieve5A, PoraPlot-Q glass capillary, and CP-Sil modules. Qualitative analysis of water concentration was done in the PoraPlot-Q channel. Appropriate sealing was confirmed by measuring the helium tracer concentration in the permeate stream. An acceptable sealing was achieved when the helium concentration was lower than 5% of the H_2 permeated. Feed humidification was accomplished by saturation at 20 °C using Milli-Q water. Data reported in the present study were recorded at a steady state after thirty minutes of stabilization, and each test has been repeated three times to minimize analysis error, obtaining an experimental standard deviation of 10^{-4}.

Stability tests in CO_2 and other acid atmospheres. Chemical stability of $BaZr_{1-x-y}Y_xM_yO_3$ powders was tested against reducing atmospheres. Two sets of experimental conditions were selected:

(1) Treatment in a continuous gas flow of 10% CO_2 and 90% CH_4, both dry and humidified (2.5% water) at 700 °C and 800 °C for 72 h.

(2) Treatment under continuous gas flow composed of 115 ppm H_2S, 4.43% CO_2, 2.12% CO and 92.09% H_2 at 500 °C, 30 bars, for 40 h.

The stability was controlled by XRD analysis before and after the treatments in order to observe microstructural and/or phase changes in the materials as a result of this short-term reduction of environmental exposure.

In addition, thermogravimetric (TG) measurements were performed on powder samples exposed to dry CO_2 (5% in Ar) flow in the temperature range from 25 °C to 1000 °C with a heating ramp of 10 K min^{-1}. For this purpose a Metler-Toledo StarE balance was used.

In order to check the *in situ* changes of the powders, Raman spectra were gathered using a CCR1000 Linkan Raman stage. The $BaZr_{1-x-y}Y_xM_yO_3$ powders were heated up to 850 °C in oxygen, then the atmosphere was changed to 15% CO_2 in Ar and then cooled down to 25 °C without changing the gas environment. Raman analysis was performed with a Renishaw inVia Raman spectrometer equipped with a Leica DMLM microscope and a 514 nm Ar^+ ion laser as an excitation source. A ×50 objective of 8 mm optical length was used to focus the depolarized laser beam on a spot of 3 μm in diameter. A CCD array detector was used for collection of the Raman scattering.

3. Results and discussion

$BaZr_{0.9}Y_{0.1}O_{3-\delta}$ was doped with Pr, Fe and Mn, aiming to modify the initial structure and create chemical defects, as well as to test the electrochemical and transport properties of the parent compound. Furthermore, in the Mn-doped compound the quantity of Y was also increased, aiming to improve specifically the protonic conductivity. For these reasons the selected compositions for this study were: $BaZr_{0.9}Y_{0.1}O_{3-\delta}$, $BaZr_{0.85}Y_{0.1}Pr_{0.05}O_{3-\delta}$, $BaZr_{0.85}Y_{0.1}Fe_{0.05}O_{3-\delta}$, $BaZr_{0.85}Y_{0.1}Mn_{0.05}O_{3-\delta}$ and $BaZr_{0.8}Y_{0.15}Mn_{0.05}O_{3-\delta}$.

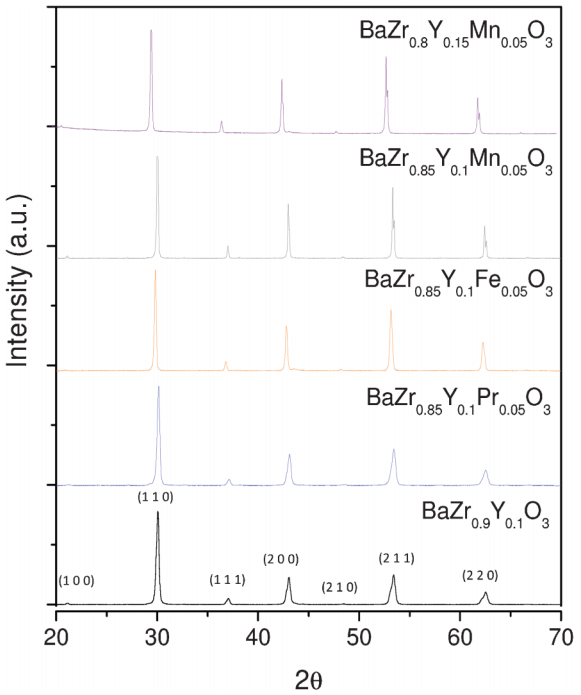

Fig. 2 XRD patterns of the $BaZr_{0.9}Y_{0.1}O_{3-\delta}$, $BaZr_{0.85}Y_{0.1}Pr_{0.05}O_{3-\delta}$, $BaZr_{0.85}Y_{0.1}Fe_{0.05}O_{3-\delta}$, $BaZr_{0.85}Y_{0.1}Mn_{0.05}O_{3-\delta}$, and $BaZr_{0.8}Y_{0.15}Mn_{0.05}O_{3-\delta}$, as sintered at 1400 °C.

3.1. Structural and microstructural characterization

Crystal structure and phase composition. XRD patterns of the selected samples after sintering are shown in Fig. 2. It can be observed that all compounds present a crystalline cubic perovskite structure as the nominally undoped $BaZrO_3$.[28] The calculated unit cell parameters, *a*, are summarized in Table 1. The variations in cell parameter are small, and therefore the possible changes in transport properties, especially those related to the oxide-ion transport, may hardly be attributed to these cell volume changes.

3.2. Electrochemical characterization

Conductivity as a function of pO_2. The influence of variation in oxygen partial pressure (pO_2) on the total conductivity was

Table 1 Lattice parameter values determined at room temperature (RT) obtained from XRD analysis after sintering at 1700 °C of the compounds in the $BaZr_{1-x-y}Y_xM_yO_{3-\delta}$-series, as well as literature data of nominally undoped $BaZrO_3$

Compound	Sample name	Lattice parameter *a*/Å at RT
$BaZrO_3$[28]	BZ	4.1913
$BaZr_{0.95}Y_{0.1}O_{3-\delta}$	BZY	4.1968
$BaZr_{0.85}Y_{0.1}Pr_{0.05}O_{3-\delta}$	BZYP	4.1993
$BaZr_{0.85}Y_{0.1}Fe_{0.05}O_{3-\delta}$	BZYF	4.2162
$BaZr_{0.85}Y_{0.1}Mn_{0.05}O_{3-\delta}$	BZYM1	4.2048
$BaZr_{0.8}Y_{0.15}Mn_{0.05}O_{3-\delta}$	BZYM2	4.2185

studied (Fig. 3) in the range 2×10^{-5} to 1 atm for the five selected compounds at three fixed temperatures (600, 700 and 800 °C). From the figure it is clearly visible that, within the experimental pO_2 range, the total conductivity of the tested samples increases with increasing pO_2. This behaviour suggests that the compounds exhibit predominantly p-type electronic conductivity. The conductivity increase observed for samples $BaZr_{0.9}Y_{0.1}O_{3-\delta}$ and $BaZr_{0.85}Y_{0.1}Pr_{0.05}O_{3-\delta}$ is of a more pO_2-dependent character than for the Fe-doped and the two Mn-doped compounds. The slope of ¼ is in agreement with the p-type behavior reported elsewhere for similar compounds.[29] For samples $BaZr_{0.85}Y_{0.1}Fe_{0.05}O_{3-\delta}$ $BaZr_{0.85}Y_{0.1}Mn_{0.05}O_{3-\delta}$ and $BaZr_{0.8}Y_{0.15}Mn_{0.05}O_{3-\delta}$, the pO_2-dependence of conductivity exhibits smaller slopes. This dependence on pO_2 can be explained by taking into account basic defect chemistry equations, which are summarized in Table 2, written in Kröger–Vink notation.

Let us consider the compound $BaZr_{0.9}Y_{0.1}O_{3-\delta}$, called *reference* in the present study, in order to introduce the defect model. When Zr is partially replaced by a trivalent cation, such as Y^{3+}, the oxygen vacancies are concurrently generated to compensate for the negative acceptor charge introduced by the incorporation of Y^{3+} in the Zr^{4+} position, as it is expressed in eqn (4):

$$Y_2O_3 \xrightarrow{BaZrO_3} Ba_{Ba}^{x} + 2Y_{Zr}^{'} + v_O^{\cdot\cdot} \quad (4)$$

The electroneutrality condition can be then expressed by eqn (5).

$$[Y_{Zr}^{'}] + 2[O_i^{''}] + n = 2[v_o^{\cdot\cdot}] + p \quad (5)$$

By substituting into the defect equations (eqn (4)), in the high pO_2 range, it is found that the concentration of electron holes is proportional to pO_2 with a slope of ¼, *e.g.* $p \propto pO_2^{1/4}$. The ionic conductivity is, furthermore, independent of pO_2, in accordance with the term ($\sigma_i \propto pO_2^0$).

With respect to the incorporation of a multivalent dopant such as Pr, the oxidation state changes (*e.g.* Pr^{3+} and Pr^{4+}) depending on pO_2 and the temperature. Subsequently, two different cases can be distinguished: (1) when Pr exists as Pr^{4+} (extreme oxidizing conditions), it does not contribute to the formation of new defects in the $BaZr_{0.9}Y_{0.1}O_{3-\delta}$ parent compound; (2) when Pr exists as Pr^{3+}, it generates oxygen vacancies following the same defect chemistry as in the case of Y-doped $BaZrO_3$. The total nominal concentration of the formed charge-compensating defects is then higher than in the single acceptor dopant (as Y) initially used in the reference compound. Due to the reversibility of the oxidation state of these cations under given environmental conditions, charge compensation can also take place by the generation or annihilation of electrons or electrons holes, which results in substantial changes in electronic conductivity. As a consequence, the electroneutrality conditions may be formulated accordingly (eqn 6):

$$[Y_{Zr}^{'}] + 2[O_i^{''}] + [Pr_{Zr}^{'}] + n = 2[v_o^{\cdot\cdot}] + p \quad (6)$$

In the same way it is found that the concentration of electron holes is proportional to pO_2 with a slope of ¼.

Another issue is dopant trapping, which is usually more pronounced when multi-dopant schemes or higher doping concentrations are used. Moreover, in multi-dopant compounds, acceptor doping effects (Y) and donor doping effects (Pr) may

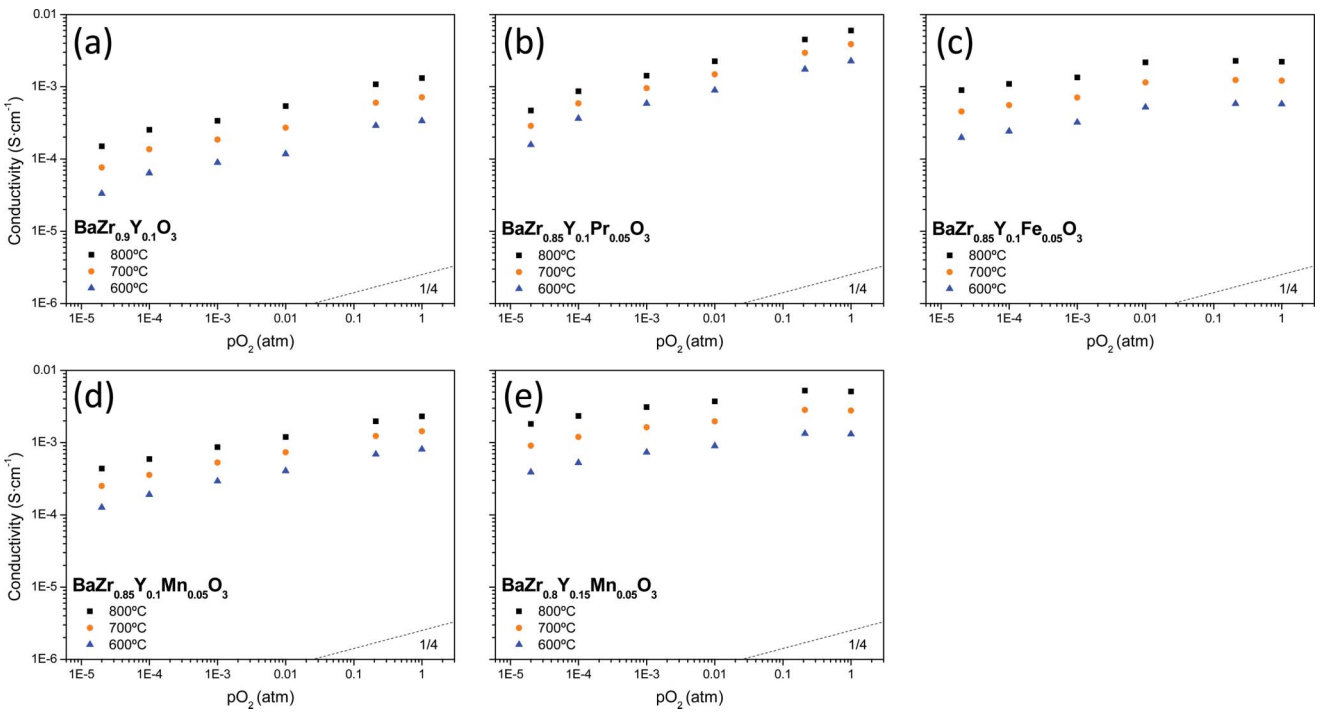

Fig. 3 Total conductivity as a function of pO_2 measured for five different compounds under dry conditions: (a) $BaZr_{0.9}Y_{0.1}O_{3-\delta}$, (b) $BaZr_{0.85}Y_{0.1}Pr_{0.05}O_{3-\delta}$, (c) $BaZr_{0.85}Y_{0.1}Fe_{0.05}O_{3-\delta}$, (d) $BaZr_{0.85}Y_{0.1}Mn_{0.05}O_{3-\delta}$ and (e) $BaZr_{0.8}Y_{0.15}Mn_{0.05}O_{3-\delta}$.

Table 2 Defect chemistry equations

Defect chemistry equations		
$O_o^x \leftrightarrow v_o^{\cdot\cdot} + O_I''$	$K_F(T) = [v_o^{\cdot\cdot}] \times [O_I'']$	(1)
nill $\leftrightarrow e' + h^{\cdot}$	$Ke(T) = n \times p$	(2)
$O_o^x \leftrightarrow 1/2\ O_2(g) + v_o^{\cdot\cdot} + 2e'$	$K_R(T) = [v_o^{\cdot\cdot}] \times n^2 \times pO_2^{1/2}$	(3)

compensate depending on dopant concentration and environmental conditions.

In the case of Fe and Mn cations used as dopants in the referent $BaZr_{0.9}Y_{0.1}O_{3-\delta}$ compound, a slightly different defect chemistry situation can be considered as they can also be in the +2 oxidation state, along with the previously discussed +3 and +4 states. In this case, the electroneutrality condition can be expressed by eqn (7) and eqn (8) for Fe and Mn, respectively.

$$[Y_{Zr}'] + 2[O_i''] + [Fe_{Zr}'] + [Fe_{Zr}''] + n = 2[v_o^{\cdot\cdot}] + p \quad (7)$$

$$[Y_{Zr}'] + 2[O_i''] + [Mn_{Zr}'] + 2[Mn_{Zr}''] + n = 2[v_o^{\cdot\cdot}] + p \quad (8)$$

As has been mentioned above, Fe and Mn doped compounds exhibit conductivity that is slightly less dependent on the pO_2 than those having a slope of ¼ (Fig. 3). This effect can be ascribed to a transition situation between the two limiting defect states, the pure p-type electronic regime (with $pO_2^{1/4}$ dependency) and the pure ionic regime (independent of pO_2).

Conductivity measurements as a function of temperature. A study of conductivity as a function of temperature was carried out in dry and humidified atmospheres (2.5% H_2O or 2.5% D_2O), in order to determine the hydration and isotopic effects in oxidizing (O_2) and reducing (5% H_2–95% He and 5% D_2–95% He) atmospheres.

Fig. 4 depicts total conductivity against inverse temperature in dry O_2, O_2 + 2.5% H_2O and O_2 + 2.5% D_2O for the five studied compounds. Two different trends in the behavior can be observed depending on the temperature range:

1. Predominant protonic conductivity at low temperatures: the hydration effect $\sigma_{O_2+H_2O} > \sigma_{O_2}$ and the isotopic effect $\sigma_{O_2+H_2O} > \sigma_{O_2+D_2O}$ are evident for all tested compounds below 600 °C.

2. Predominant p-type and oxygen-ion conductivity at high temperatures: in these conditions the hydration and isotopic effects become negligible. This behavior is evident in the five tested compounds at temperatures above 600 °C due to oxide dehydration.

The same trends were observed for the measurements carried out in dry and wet helium (Fig. S1, ESI†). Furthermore, conductivity values in dry reducing (5% H_2 and 5% D_2) and wet reducing (5% H_2 + 2.5% H_2O and 5% D_2 + 2.5% D_2O) atmospheres are shown in Fig. 5 as a function of temperature. These conditions are the most relevant for practical application as H_2-permeable membranes. It can be noticed that, in all studied compounds, protonic conduction prevails across the whole range of temperatures. This behavior can be inferred from the hydration effect ($\sigma_{O_2+H_2O} > \sigma_{O_2}$) and the isotopic effect ($\sigma_{H_2+H_2O} > \sigma_{D_2+D_2O}$) observed for all tested compounds.

At the highest temperature tested, the change in activation energy is related to the depletion of protons in the oxide and, as a consequence, the contribution of electrons and especially oxide ions becomes more relevant with the increase in temperature. Thus, the activation energy for proton and deuterium diffusion can be determined from the low temperature range (up to 600 °C) of the conductivity plots. Table 3 summarizes the activation energy values of the different compounds measured in oxidizing conditions. The very high values of these activation energies can be related to the grain boundary reported values,[25,26] due to the limiting grain boundary resistivity for proton transport of this kind of material, deduced from the reported impedance studies.[24–26] Furthermore, the activation energy for deuterium diffusion is about 0.04–0.08 eV higher than for protons (except for the Pr doped compound, which is higher). This difference is expected due to the lower zero point energy for deuterium ions than for protons.[30]

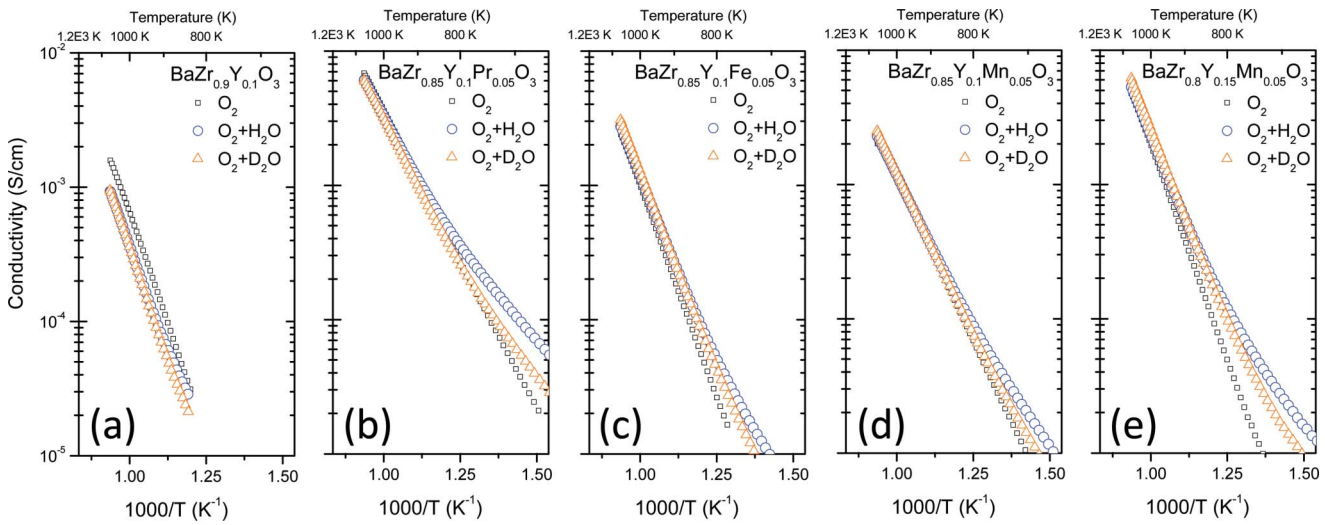

Fig. 4 Total conductivity as a function of inverse temperature measured in dry oxygen, oxygen saturated with water and oxygen saturated with deuterated water: (a) $BaZr_{0.9}Y_{0.1}O_{3-\delta}$, (b) $BaZr_{0.85}Y_{0.1}Pr_{0.05}O_{3-\delta}$, (c) $BaZr_{0.85}Y_{0.1}Fe_{0.05}O_{3-\delta}$, (d) $BaZr_{0.85}Y_{0.1}Mn_{0.05}O_{3-\delta}$ and (e) $BaZr_{0.8}Y_{0.15}Mn_{0.05}O_{3-\delta}$. Saturation with H_2O and D_2O was carried out at room temperature.

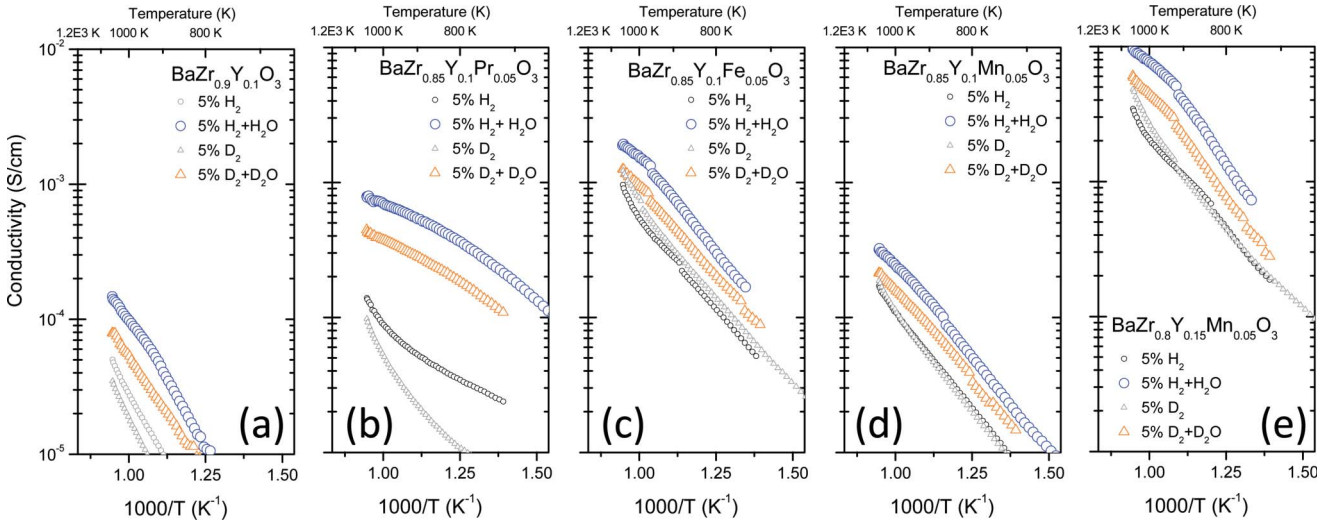

Fig. 5 Total conductivity as a function of inverse temperature measured in hydrogen saturated with water and deuterium saturated with deuterated water for five different compounds: (a) $BaZr_{0.9}Y_{0.1}O_{3-\delta}$, (b) $BaZr_{0.85}Y_{0.1}Pr_{0.05}O_{3-\delta}$, (c) $BaZr_{0.85}Y_{0.1}Fe_{0.05}O_{3-\delta}$, (d) $BaZr_{0.85}Y_{0.1}Mn_{0.05}O_{3-\delta}$ and (e) $BaZr_{0.8}Y_{0.15}Mn_{0.05}O_{3-\delta}$. Saturation with H_2O and D_2O was carried out at room temperature.

Table 3 Proton and deuterium activation energies calculated from the conductivity Arrhenius plots of the different compounds showed in Fig. 4

Compound	O_2+H_2O E_a (eV)	O_2+D_2O E_a (eV)
$BaZr_{0.95}Y_{0.1}O_{3-\delta}$	1.35	1.44
$BaZr_{0.85}Y_{0.1}Pr_{0.05}O_{3-\delta}$	0.79	1.02
$BaZr_{0.85}Y_{0.1}Fe_{0.05}O_{3-\delta}$	0.68	0.75
$BaZr_{0.85}Y_{0.1}Mn_{0.05}O_{3-\delta}$	0.92	1.01
$BaZr_{0.8}Y_{0.15}Mn_{0.05}O_{3-\delta}$	0.92	0.97

We should also emphasize the important improvement in total conductivity with increase in Y concentration, *i.e.* the change from $BaZr_{0.85}Y_{0.1}Mn_{0.05}O_{3-\delta}$ to $BaZr_{0.8}Y_{0.15}Mn_{0.05}O_{3-\delta}$. Indeed, impedance analysis of $BaZr_{0.8}Y_{0.15}Mn_{0.05}O_{3-\delta}$ at 300 °C in dry and wet hydrogen (4% in Ar) revealed that the most important contribution to the total sample resistance is the one related to grain boundary transport (Fig. S2, ESI†). Moreover, it should be noted that our $BaZr_{0.9}Y_{0.1}O_{3-\delta}$ reference compound shows total conductivity values lower than those reported elsewhere[24–26] and this might be ascribed to (i) barium evaporation, (ii) non-stoichiometry, (iii) core-space charge layer effects, *etc.*[25] Nevertheless, the best material found here ($BaZr_{0.8}Y_{0.15}Mn_{0.05}O_{3-\delta}$) exhibits a conductivity almost two orders of magnitude higher than our reference compound ($BaZr_{0.9}Y_{0.1}O_{3-\delta}$). Furthermore, the protonic conductivity is enhanced in the Y-doped compound, as can be deduced from the higher magnitude of the isotopic effect in $BaZr_{0.8}Y_{0.15}Mn_{0.05}O_{3-\delta}$ than in $BaZr_{0.85}Y_{0.1}Mn_{0.05}O_3$. This fact is in agreement with previously reported studies[31] and can be directly ascribed to the higher density of oxygen vacancies created by the substitution of Zr by Y, essential for the incorporation of protons in the oxide. As the protonic conductivity in these polycrystalline samples is principally limited by grain boundary resistance,[24–26] the observed conductivity improvements should be a consequence of better grain boundary transport of both ions and electronic charge carriers achieved through the variation in composition.

Aiming to understand the evolution of the Mn-oxidation state in $BaZr_{0.8}Y_{0.15}Mn_{0.05}O_{3-\delta}$ under reducing conditions, a temperature-programmed reduction (TPR) experiment was carried out in dry hydrogen. Fig. 6 presents the weight-normalized hydrogen consumption for $BaZr_{0.9}Y_{0.1}O_{3-\delta}$ and $BaZr_{0.8}Y_{0.15}Mn_{0.05}O_{3-\delta}$. The reference samples presents some background reduction in the temperature range 450 to 900 °C, which can be ascribed to oxygen release and the formation of electron carriers upon oxide dehydration. In the case of $BaZr_{0.8}Y_{0.15}Mn_{0.05}O_{3-\delta}$, two additional pronounced reduction peaks are observed. The low temperature peak detected at 415 °C is related to the reduction of Mn^{4+} to Mn^{3+} and the consequent formation of the oxygen vacancies and water, which is in agreement with previous studies on $La_{1-x}Ca_xMnO_{3-\delta}$ perovskites.[32,33] The reduction process taking place at 788 °C is related to the subsequent reduction of Mn^{3+} to Mn^{2+} and consumes a larger amount of hydrogen than the low temperature reduction. From the hydrogen consumption values, it can be inferred that Mn^{2+}-ions are the prevailing species at temperatures above 900 °C in dry hydrogen while Mn^{4+}-ions represent around 30%

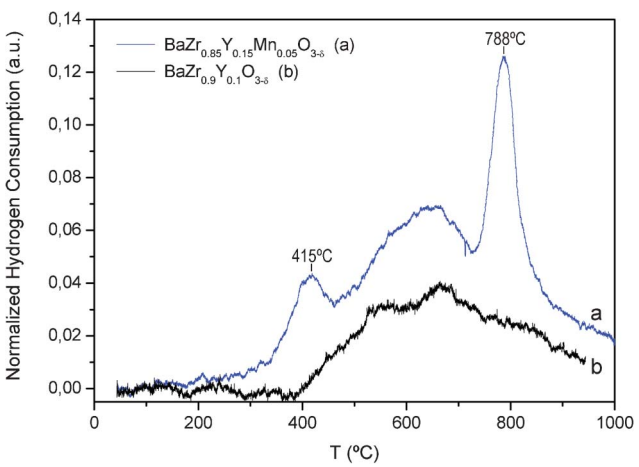

Fig. 6 Temperature-programmed reduction experiment in dry H_2 (10% in Ar) for $BaZr_{0.9}Y_{0.1}O_{3-\delta}$ and $BaZr_{0.8}Y_{0.15}Mn_{0.05}O_{3-\delta}$ compounds.

of the lattice Mn in perovskite at temperatures below 350 °C. Under the usual membrane operating conditions (750–1000 °C), Mn cations can be easily reduced or oxidized, depending on the specific temperature, pH_2 and pH_2O, which in turn can promote both the n-type electronic conduction and redox surface catalysis.

3.3. H_2 permeation study

Hydrogen flux through the $BaZr_{0.8}Y_{0.15}Mn_{0.05}O_{3-\delta}$ membrane was studied as a function of several parameters as considered below.

Flux *versus* degree of humidification. In order to study the hydration effect on the flux through the membrane, and also to prove the eventual water splitting contribution in the sweep side as suggested in ref. 34, the humidification degree was varied and the impact on the hydrogen evolution rate was investigated. Two limiting cases were selected for variation of the humidification degree, *i.e.* configuration one (C1): only the feed side of the membrane was humidified; and configuration two (C2): both membrane sides were simultaneously humidified (pH_2O = 0.025 atm). The tests were done using a mixture of 50% H_2 in helium as the feed gas.

Fig. 7a shows hydrogen permeation fluxes of both configurations (hydration degree configurations) as a function of temperature, using 50% H_2 as the feed gas. A clear improvement in hydrogen flux through the membrane can be observed when both sides are humidified due to (1) better hydration of the membrane, which results in a higher proton concentration across the membrane, especially in the region close to the permeate; and (2) the positive contribution of the oxide-ion transport in the direction of the feed, which leads to the formation of hydrogen in the permeate side, thanks to the water splitting process. Indeed, the pO_2 gradient across the membrane and the associated oxide-ion transport direction are reversed when sweep gas is humidified. Therefore, when the sweep is dry (C1), part of the protons diffusing towards the permeate recombine with oxide-ions to form water and the net hydrogen flow is diminished. A similar behavior was previously observed in other hydrogen-permeable ceramic membranes.[34]

Fig. 7b represents the transient process recorded at 1000 °C when switching from configuration C1 to C2. In the initial configuration with the dry sweep gas (C1), the hydrogen flux is lower than 0.01 ml min^{-1} cm^{-2} and the hydrogen flow increases steeply before reaching a peak value of 0.8 ml min^{-1} cm^{-2} upon switching to humidified sweep gas (C2). Nevertheless, the flow decreases drastically with time and after ~100–150 min it stabilizes at around 0.03 ml min^{-1} cm^{-2}, as can be seen in Fig. 7b. This temporary increase in hydrogen flux cannot be only attributed to the aforementioned higher membrane degree of hydration and simple water splitting effects on the sweep side. A plausible explanation is the potential partial oxidation of the membrane material when pO_2 is increased on the sweep side, as a consequence of the addition of water. This oxidation could originate from the redox activity of Mn cations in this temperature range, involving the oxidation from Mn^{2+} to Mn^{3+}. Therefore, it may be suggested that the initially observed increase in H_2 flow to peak values of ~0.8 ml min^{-1} cm^{-2} stems from coupled water splitting and membrane oxidation processes.

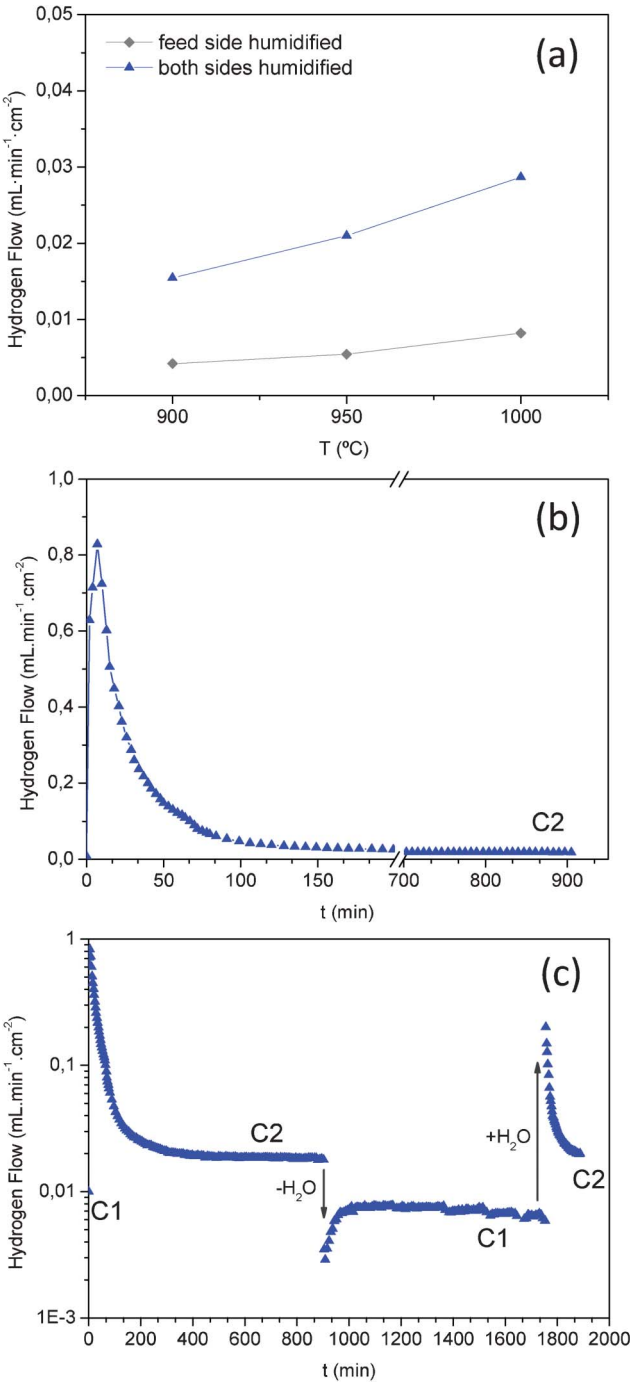

Fig. 7 Hydrogen flux through the $BaZr_{0.8}Y_{0.15}Mn_{0.05}O_{3-\delta}$ membrane: (a) flux as a function of temperature in two configurations: (i) when the feed side was humidified and (ii) when both feed and sweep sides of the membrane were humidified (the measurements were performed with a mixture of 50% H_2 in He as the feed gas); (b) time stabilization of hydrogen flux at 1000 °C when the sweep gas is switched from wet to dry argon; and (c) flux at 1000 °C as a function of time, with several transitions from wet to dry argon sweep and *vice versa*. (Stages where water was added or removed are additionally notified by arrows.)

Hence, the transient profile may be related to oxide-ion diffusion into the membrane. Moreover, in the steady state (C2), a graded concentration of Mn^{2+} and Mn^{3+} across the membrane would be expected from the applied pO_2 gradient. Finally, this mechanism

suggests that the humidification of the sweep induces several changes in the membrane material, that is, it alters the hydration degree, the concentration of oxygen vacancies and the concentration of electron carriers (n).

The study of the flux evolution at 1000 °C when the hydration configuration is successively changed (C1↔C2) is represented in Fig. 7c (note the logarithmic scale). Three different steps are plotted: (1) when both sides are humidified (C1→C2), the hydrogen flow passes through a maximum and then with time stabilizes around 0.03 ml min^{-1} cm^{-2}; (2) when the sweep side is dried (C2→C1), the flux drops drastically, but later it increases slowly before reaching values lower than 0.01 ml min^{-1} cm^{-2} and finally (3) when the sweep side is humidified again (C1→C2), hydrogen flux increases quickly reaching a maximum and then the flow stabilizes at the same value as in the first step, around 0.03 ml min^{-1} cm^{-2}.

The steep drop in hydrogen flow is consistent with the proposed transient mechanism and in this step change the membrane is reduced again, *i.e.* Mn^{3+} to Mn^{2+}, consuming part of the hydrogen permeated during this temporary process. Moreover, the possible interpretation of the observed drastic drop in H_2 flow due to the eventual degradation effects under the test conditions is ruled out, since this drop could be repeated in successive gas environment step changes and because of the reversibility of the process. Additionally, the results of the SEM and TEM studies support the membrane stability after the permeation test and allow the rejection such a possibility for explaining the observed flux degradation (see SEM and TEM images in Fig. 9 and 10, respectively).

Flux *versus* temperature and pH_2. Once hydrogen flux was stabilized at 1000 °C, the permeation was measured as a function of the temperature and also the effect of the feed stream concentration was studied. Three different feed compositions (pH_2) were selected: 0.05, 0.2 and 0.5 atm while both membrane sides were humidified (pH_2O = 0.025 atm). Fig. 8 illustrates the temperature dependence of hydrogen flux at the three different feed concentrations. It can be seen that the hydrogen flux increases with increasing pH_2 and temperature, as is postulated by Wagner theory.[35] Specifically, the hydrogen flow at 1000 °C seems to follow a linear dependence when it is represented as a function of $p_{H2,feed}^{0.5} - p_{H2/perm}^{0.5}$ (see inset in Fig. 8), which suggests that the majority of the charge carriers are protons and oxide-ions, and electrons are still limiting the ambipolar conductivity, as previously inferred from the conductivity measurements in reducing conditions (Fig. 5).

Based on the permeation measurements carried out in this work, and also considering Wagner theory, a flux of 7 ml min^{-1} cm^{-2} at 900 °C may be predicted for 20 μm-thick $BaZr_{0.8}Y_{0.15}M_{0.05}O_{3-\delta}$ membranes. When compared to the H_2-flux measured for selected state-of-the art materials, *e.g.* 0.102 ml min^{-1} cm^{-2} for a 50 μm-thick $SrCe_{0.95}Y_{0.05}O_{3-\delta}$ membrane at 950 °C (80% H_2–He upstream and Ar downstream)[36,37] or 13.44 ml min^{-1} cm^{-2} for a 2 μm-thick $SrCe_{0.95}Yb_{0.05}O_{3-\delta}$ membrane at 677 °C (H_2 upstream and He downstream),[38] the predicted value seems to be very promising. Therefore, $BaZr_{0.8}Y_{0.15}M_{0.05}O_{3-\delta}$ can be pointed out as an attractive membrane material for H_2-separation at elevated temperatures.

After hydrogen permeation measurements, the sample was analyzed by SEM, in order to check the stability of these compounds in humidified reducing conditions. Fig. 9 shows SEM images of the polished cross-section $BaZr_{0.8}Y_{0.15}Mn_{0.05}O_{3-\delta}$ membrane after the conductivity test, and no degradation or secondary phases in the membrane interior were detected. The average grain size is around 1 μm for the fresh and treated samples while the grain size for the $BaZr_{0.85}Y_{0.1}Mn_{0.05}O_{3-\delta}$ compound is slightly higher, around 2 μm. All investigated samples presented a very high density with very good attachment between grains and only small and scarce occluded pores can be found.

Fig. 10 presents a transmission electron microscopy (TEM) study of the membrane region close to the surface exposed to the sweep side during the permeation test. Fig. 10c shows a micrograph of the cross section of the sample. Grains of 400 nm to 2 μm in diameter are present within the specimen. In Fig. 10a a sample area with larger magnification is visible, which lies approximately 2 μm below the sample surface. Neither secondary phases nor precipitates can be observed within the grains or at the grain boundaries, which confirms the total solution of the Y and Mn dopants, as suggested by the previous XRD analysis. Fig. 10b shows the sample at the specimen surface. The inhomogeneous layer at the top of the image corresponds to the residue of a platinum covering layer, which was deposited onto the sample during the specimen-preparation procedure. Between the covering layer and the sample a thin carbon layer (10–20 nm in thickness) with bright contrast is visible. Additionally, an enhanced surface roughness can be observed, which is considered to be a result of the permeation measurements. In line with this observation, Fig. 10d shows an SEM image of the top surface of the membrane. Grain boundaries cannot be distinguished in this micrograph, due to the surface roughness and the carbon layer. Occasionally, particles are observed on top of the surface of the membrane, which may originate from deposition of dust or particulate from piping and upstream setup components. This kind of surface foiling was previously reported for high temperature membranes tested in a similar experimental setup.[39]

3.4. Stability in reducing and CO_2-rich environments

Fig. 11 shows the XRD patterns of the zirconate samples developed in this study and a reference sample made of Eu-doped $BaCeO_3$. The short-term stability test was carried out on samples previously calcined at 1400 °C for 8 h. The powder samples were exposed to a continuous gas flow composed of 10% CO_2 and 90% CH_4 at 800 °C for 72 h. These conditions were selected in order to simulate the relevant hydrogen separation conditions, *i.e.* moist CO_2-rich reducing atmospheres at elevated temperature. The temperature of 800 °C is high enough to test the samples against carbonate formation but still below the limit of carbonate decomposition. As seen from the figure, all tested zirconate samples remained apparently unchanged after treatment under the test conditions, while the Eu-doped $BaCeO_3$ sample fully decomposed due to the formation of barium carbonates.

In a second stability test, the materials developed in this study were exposed for 40 h under the action of a continuous gas flow

‡ $j_H{}^+ = \frac{RT}{2F^2L}\frac{\sigma_H\sigma_g}{\sigma_{COC}}\left[p_{H2,feed}^{0.5} - p_{H2,perm}^{0.5}\right] + \frac{RT}{2F^2L}\frac{\sigma_H\sigma_{ox}}{\sigma_{COC}}\left[p_{H2,feed}^{0.5} - p_{H2,perm}^{0.5}\right]$

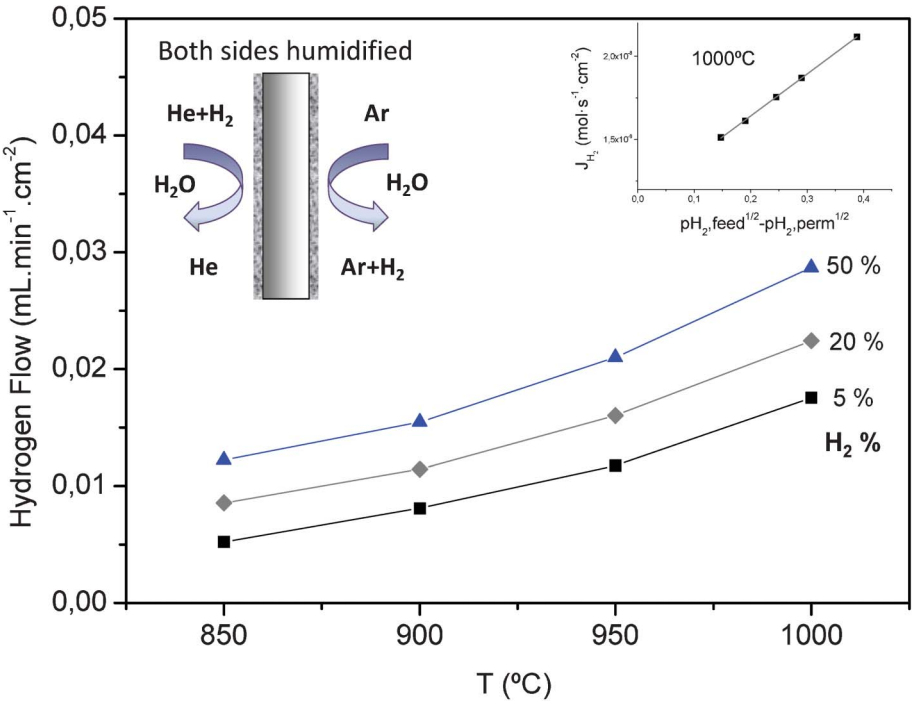

Fig. 8 Hydrogen flux through the $BaZr_{0.8}Y_{0.15}Mn_{0.05}O_{3-\delta}$ membrane as a function of temperature and hydrogen partial pressure when both sides (feed and sweep) of the membrane are humidified.

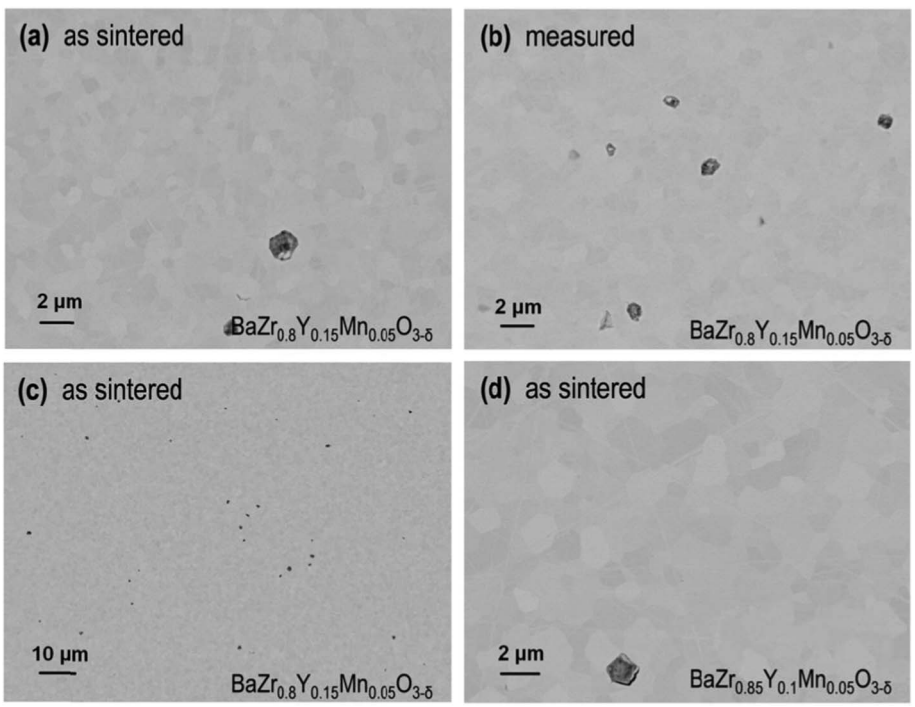

Fig. 9 SEM images of polished cross-sections of the $BaZr_{0.8}Y_{0.15}Mn_{0.05}O_{3-\delta}$ membrane before and after the hydrogen permeation test.

composed of 115 ppm H_2S, 4.43% CO_2, 2.12% CO and 92.09% H_2 at 500 °C, 30 bars and the phase composition was controlled *via* the XRD. Pre- and post-treatment XRD-patterns are presented in Fig. 12. No secondary phases can be observed in the case of zirconates also for this set of experimental conditions. Nevertheless, the Eu-doped $BaCeO_3$ decomposed again, forming barium carbonates and cerium-rich sulfates.

In order to ensure the stability of zirconates in CO_2-containing atmospheres, the different materials were additionally studied by thermogravimetry (TG). TG curves (Fig. 13) were recorded for $BaZr_{0.9}Y_{0.1}O_{3-\delta}$, $BaZr_{0.8}Y_{0.15}Mn_{0.05}O_{3-\delta}$ and $BaCe_{0.9}Yb_{0.1}O_{3-\delta}$ under continuous gas flow of a mixture of 5% CO_2, while the temperature was raised up to 1000 °C. For all studied samples, a small weight loss was observed with temperature increase up to

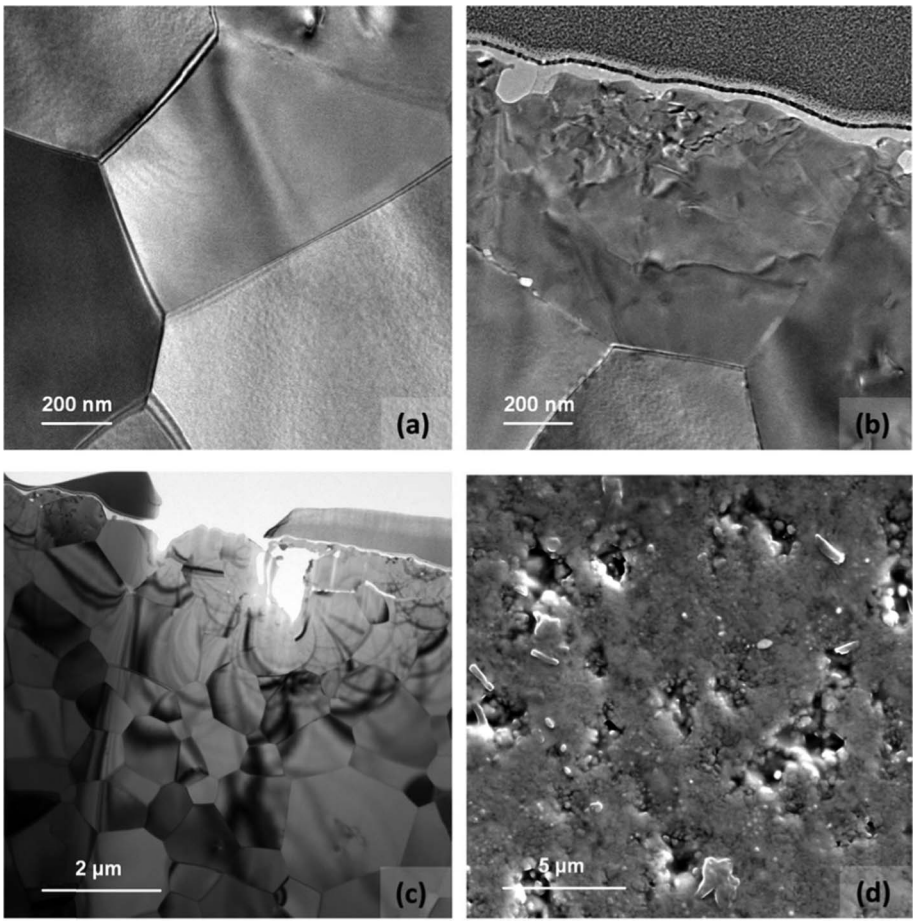

Fig. 10 (a, b, c) TEM study of $BaZr_{0.8}Y_{0.15}Mn_{0.05}O_{3-\delta}$ membrane after the hydrogen permeation test and (d) SEM analysis of the membrane surface exposed to the sweep after the permeation test.

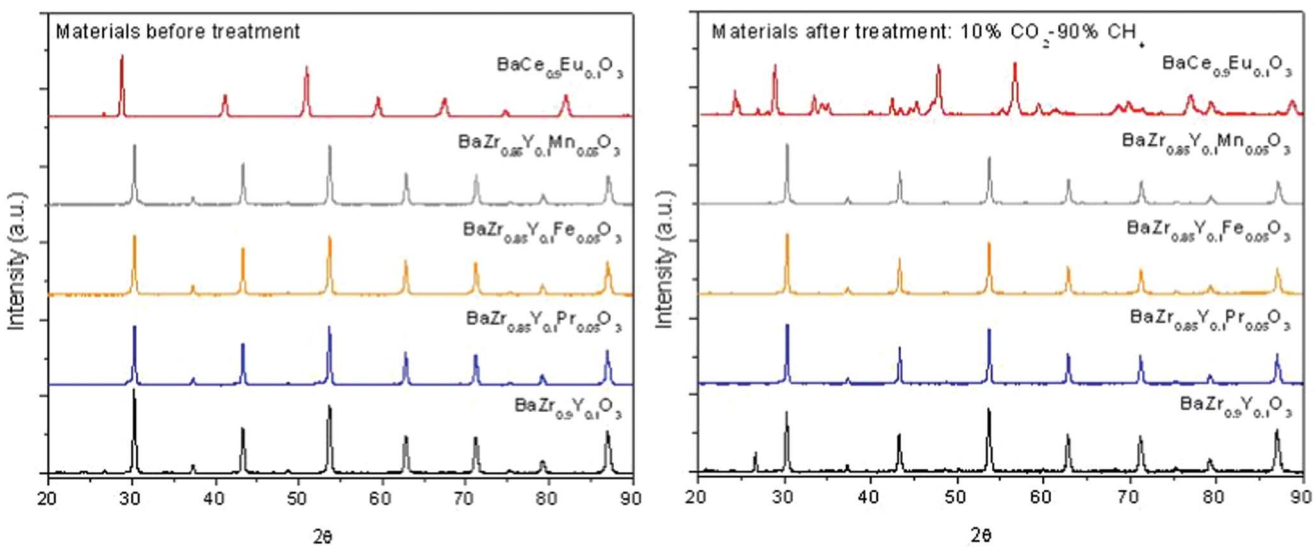

Fig. 11 XRD diffraction patterns of compounds from the $BaZr_{1-x-y}Y_xM_yO_{3-\delta}$-series before and after the stability test in a mixture of 10% CO_2 and 90% CH_4 carried out at 800 °C for 72 h. The XRD diffraction pattern of $BaCe_{0.9}Eu_{0.1}O_{3-\delta}$ was added for comparison.

500 °C, which may be attributed to sample dehydration and slight oxygen release, as also discussed in the conductivity measurements section. $BaCe_{0.9}Yb_{0.1}O_{3-\delta}$ shows a gradual weight gain recorded above 600 °C that can be ascribed to the formation of carbonates.[40,41] Further heating induced weight loss at 950 °C implies that the reverse reaction may have taken place, leading to release of CO_2. No reaction with CO_2 was observed in the TG curve of $BaZr_{0.9}Y_{0.1}O_{3-\delta}$ and $BaZr_{0.8}Y_{0.15}Mn_{0.05}O_{3-\delta}$.

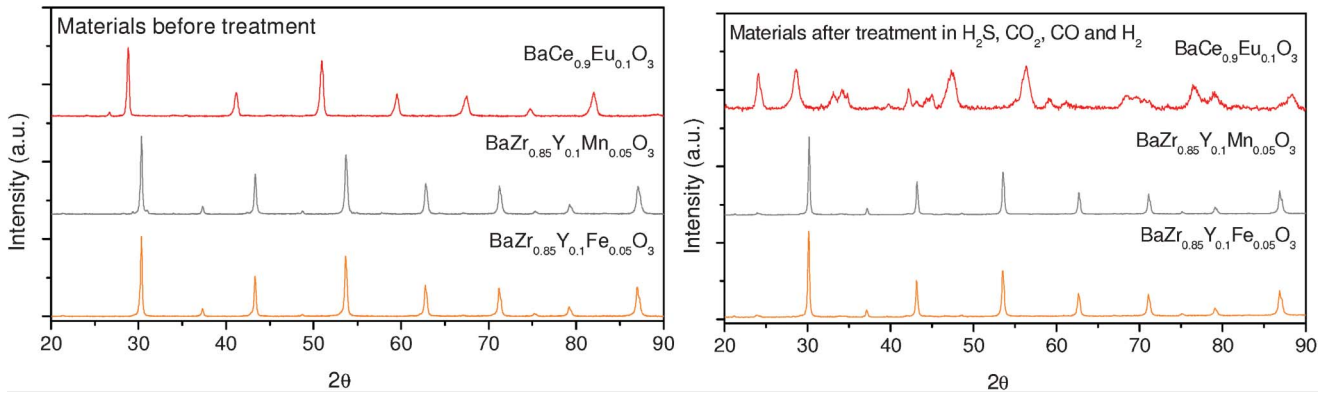

Fig. 12 XRD diffraction patterns of $BaZr_{0.85}Y_{0.1}Fe_{0.05}O_{3-\delta}$ and $BaZr_{0.8}Y_{0.15}Mn_{0.05}O_{3-\delta}$ before and after the stability test in a mixture of 115ppm H_2S, 4.43% CO_2, 2.12% CO and 92.09% H_2, carried out for 40 h at 500 °C and 30 bars. The XRD diffraction pattern of $BaCe_{0.9}Eu_{0.1}O_{3-\delta}$ was added for comparison.

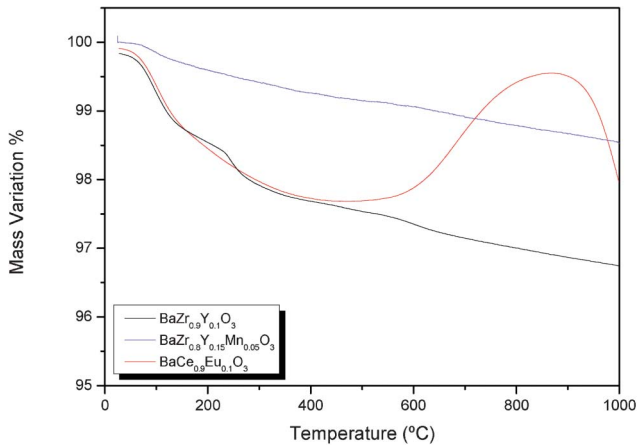

Fig. 13 TG measurements of $BaZr_{0.9}Y_{0.1}O_{3-\delta}$ and $BaZr_{0.8}Y_{0.15}Mn_{0.05}O_{3-\delta}$ in 5% CO_2 in Ar. TG data for $BaCe_{0.9}Yb_{0.1}O_{3-\delta}$ were plotted for comparison.

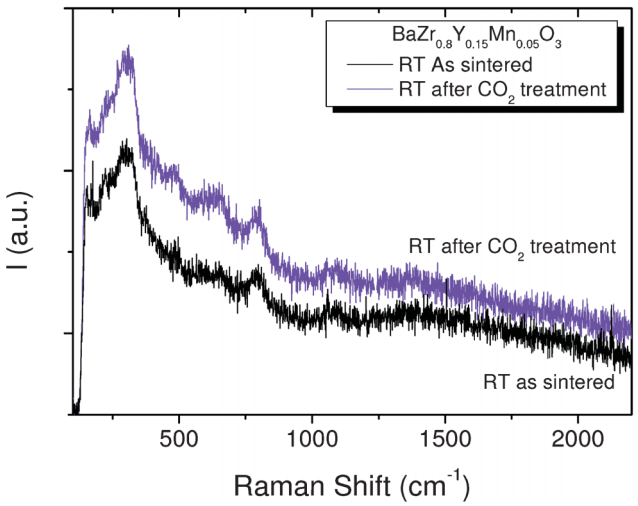

Fig. 14 Raman spectroscopy analysis carried out for the $BaZr_{0.8}Y_{0.15}Mn_{0.05}O_{3-\delta}$ sample: the black curve is for the as-sintered sample and the blue curve is for the sample being treated in a continuous flow of 15% CO_2 in Ar at 750 °C for 3 h.

Finally, Raman spectroscopy was used as a concluding technique to confirm the stability of the developed compounds in CO_2, as it can be used for *in situ* detection of carbonate formation on the perovksite surface, which are hardly detected by XRD. Results recorded for the $BaZr_{0.8}Y_{0.15}Mn_{0.05}O_{3-\delta}$ sample as sintered in air, and after exposure to a continuous flow of 15% CO_2 in Ar at 750 °C for 3 h, are presented in Fig. 14. From the experiment carried out, it can be ascertained that in this set of test conditions no formation of carbonate was observed, since the same structural peaks appear as seen in the graph. In contrast, the formation of $BaCO_3$ was observed when Yb-doped $BaCeO_3$ was exposed to the same temperature-programmed carbonation treatment as reported in ref. 34.

4. Conclusions

The present study shows structural and transport properties of Pr-, Fe-, and Mn-doped $BaZr_{1-x-y}Y_xM_yO_{3-\delta}$ compounds. Once demonstrated that the Mn-dopant leads to significant improvement in the total conductivity of the parent compound, $BaZr_{0.8}Y_{0.15}Mn_{0.05}O_{3-\delta}$ was selected for carrying out the hydrogen permeation measurements. This compound exhibited the highest total and protonic conductivities at elevated temperatures under reducing atmospheres while a particular redox behavior related to Mn species is observed under these conditions. The hydrogen permeation flow obtained through the $BaZr_{0.8}Y_{0.15}Mn_{0.05}O_{3-\delta}$ membrane was higher than previously reported for the cerates[42,43] and also comparable to other compounds, as for example solid solutions of cerates and zirconates.[44] In addition, the stability of $BaZr_{0.8}Y_{0.15}M_{0.05}O_{3-\delta}$ under operation-relevant atmospheres was studied through several techniques and the results showed unambiguously that this material has a high stability in both CO_2 and H_2S-containing operation environments. Finally, it can be pointed out that, from the developed materials in the series, $BaZr_{1-x-y}Y_xM_yO_{3-\delta}$, $BaZr_{0.8}Y_{0.15}M_{0.05}O_{3-\delta}$ is a promising candidate for industrial hydrogen-oriented applications, and competitive hydrogen flow of around 7 ml min^{-1} cm^{-2} at 900 °C could be achieved using 20 μm-thick membranes. Therefore, supported thin layer

membranes should be developed to minimize the required membrane area for the targeted industrial applications.

Acknowledgements

Financial support by the Spanish Ministry for Economics and Competitiveness (JAE-Pre 08-0058, ENE2008-06302 and ENE2011-24761 grants) and the Helmholtz Association of German Research Centers through the Helmholtz Alliance MEM-BRAIN (Initiative and Networking Fund) is kindly acknowledged. Dr M. Ivanova thanks the Northern European Innovative Energy Research Program N-INNER (grant no. 09-064274) and the German Federal Ministry of Education and Research (BMBF) for supporting the N-INNER Project "Novel High Temperature Proton and Mixed-Proton Electron Conductors for Fuel Cells and H_2-separation membranes" (Contract 03SF0330).

References

1 T. Norby and Y. Larring, *Solid State Ionics*, 2000, **136**, 139.
2 H. Iwahara, *Solid State Ionics*, 1995, **77**, 289.
3 K. D. Kreuer, *Annu. Rev. Mater. Res.*, 2003, **33**, 333–359.
4 K. H. Ryu and S. M. Haile, *Solid State Ionics*, 1999, **125**, 355.
5 P. Babilo and S. M. Haile, *J. Am. Ceram. Soc.*, 2005, **88**, 2362.
6 J. M. Serra and W. A. Meulenberg, *J. Am. Ceram. Soc.*, 2007, **90**, 2082.
7 W. A. Meulenberg, J. M. Serra and T. Schober, *Solid State Ionics*, 2006, **177**, 2851.
8 S. Ricote, G. Caboche and O. Heintz, *J. Appl. Electrochem.*, 2009, **39**, 553.
9 J. Tong, D. Clark, L. Bernau, A. A. Subramaniyan and R. O'Hayre, *Solid State Ionics*, 2010, **181**, 496.
10 S. J. Song, T. H. Lee, L. Cheng, S. E. Dorries and U. Balachandran, *US Pat.* US2010/0031822 A1 to U Chicago Argonne, LLC.
11 S.-J. Song, E. D. Wachsman, J. Rhodes, H.-S. Yoon, K.-H. Lee, G. Zhang, S. E. Dorris and U. Balachandran, *J. Mater. Sci.*, 2005, **40**, 4061.
12 H. Matsumoto, T. Shimura, T. Higuchi, H. Tanaka, K. Katahira, T. Otake, T. Kudo, K. Yashiro, A. Kaimai, T. Kawada and J. Mizusakia, *J. Electrochem. Soc.*, 2005, **152**, A488.
13 H. Matsumoto, T. Shimura, H. Iwahara and K. Katahira, *US Pat.* US2006/0157674 A1 to Nagoya University.
14 X. Wei, J. Kniep and Y. S. Lin, *J. Membr. Sci.*, 2009, **345**, 201.
15 J. Kniep and Y. S. Lin, *Ind. Eng. Chem. Res.*, 2010, **49**, 2768.
16 G. C. Mather, D. Poulidi, A. Thursfield, M. J. Pascual, J. R. Jurado and I. S. Metcalfe, *Solid State Ionics*, 2010, **181**, 230.
17 M. Y. Cai, H. X. Luo, Z. Li, A. Feldhoff, J. Caro and H. H. Wang, *Chin. Chem. Lett.*, 2008, **19**, 1256.
18 T. Oh, H. Yoon, J. Li and E.D. Wachsman, *J. Membr. Sci.*, 2009, **345**, 1.
19 Z. Sun, E. Fabbri, L. Bi and E. Traversa, *Phys. Chem. Chem. Phys.*, 2011, **13**, 7692.
20 M. Shirpour, R. Merkle and J. Maier, *Solid State Ionics*, 2011, DOI: 10.1016/j.ssi.2011.09.006.
21 D. Pergolesi, E. Fabbri, A. D'Efifanio, E. Di Bartolomeo, A. Tebano, S. Sanna, S. Licoccia, G. Balestrino and E. Traversa, *Nat. Mater.*, 2010, **9**, 846.
22 H. Iwahara, T. Esaka, H. Uchida and N. Maeda, *Solid State Ionics*, 1981, **3**, 359.
23 T. Norby and Y. Larring, *Solid State Ionics*, 1995, **77**, 147.
24 H. G. Bohn and T. Schober, *J. Am. Ceram. Soc.*, 2000, **83**, 768.
25 S. Ricote, N. Bonanos, H. J. Wang and B. A.Boukamp, *Solid State Ionics*, 2012, **213**, 36.
26 S. Ricote, N. Bonanos, A. Manerbino and W. G. Coors, *Int. J. Hydrog. Energy, in press*, DOI: 10.1016/j.ihydene.2011.08.118.
27 M. Shirpour, B. Rahmati, W. Sigle, P. A. van Aken, R. Merkle and J. Maier, *J. Phys. Chem. C*, 2012, **116**, 2453.
28 I. Levin, T. G. Amos, S. M. Bell, L. Farber, T. A. Vanderah, R. S. Roth and B. H. Toby, *J. Solid State Chem.*, 2003, **175**, 170.
29 W. Wang and A. V. Virka, *J. Power Sources*, 2005, **142**, 1.
30 A. S. Nowik and Y. Du, *Solid State Ionics*, 1997, **97**, 17.
31 K. D. Kreuer, St. Adams, W. Munch, A. Fuchs, U. Klock and J. Maier, *Solid State Ionics*, 2001, **145**, 295.
32 W. P. Stege, L. E. Cadus and B. P. Barbero, *Catal. Today*, 2011, **172**, 53.
33 S. Ponce, M. A. Peña and J. L. G. Fierro, *Appl. Catal., B*, 2000, **24**, 193.
34 S. Escolástico, C. Solís and C. J. M. Serra, *Int. J. Hydrogen Energy*, 2011, **36**, 11946.
35 H. Matsumoto, T. Shimura, H. Iwahara, T. Higuchi, K. Yashiro and A. Kaimai, *J. Alloys Compd.*, 2006, **408**, 456.
36 W. A. Meulenberg, M. Ivanova, St. Roitsch and J. M. Serra in *Advanced membrane science and technology for sustainable energy and environmental applications, Woodhead Publishing Series in Energy No. 25*, ISBN 978-1-84569-969-7, ed. Angelo Basile and Suzana Pereira Nuñes, Woodhead Publishing Limited, Cambridge, UK, 2011, ch. 17, Part IV, pp. 541–567 .
37 S. Zhan, X. Zhu, B. Ji, W. Wang, X. Zhang, J. Wang, W. Yang and L. Lin, *J. Membr. Sci.*, 2009, **340**, 241.
38 S. Hamakawa, L. Li, A. Li and E. Iglesia, *Solid State Ionics*, 2002, **148**, 71.
39 S. Baumann, J. M. Serra, P. Lobera, S. Escolástico, F. Schulze-Küppers and W. A. Meulenberg, *J. Membr. Sci.*, 2011, **377**, 198.
40 K. H. Ryu and S.M. Haile, *Solid State Ionics*, 1999, **125**, 355.
41 M. J. Scholten, J. Schoonman, J. C. Vanmiltenburg and H. A. J. Oonk, *Solid State Ionics*, 1993, **61**, 83.
42 X. Wei, J. Kniep and Y. S. Lin, *J. Membr. Sci.*, 2009, **345**, 201.
43 S. J. Song, E. D. Wachsman, J. Rhodes, S. E. Dorris and U. Balachandran, *Solid State Ionics*, 2004, **167**, 99.
44 J. Kniep and Y. S. Lin, *Ind. Eng. Chem. Res.*, 2010, **49**, 2768.